Applied Thermal Engineering 289 (2026) 129832

Contents lists available at ScienceDirect

Applied Thermal Engineering

journal homepage: www.elsevier.com/locate/ate

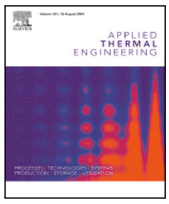

Research Paper

Effect of vacuum degradation on heat losses in parabolic trough collector receivers

Vinod Kumar [a,b], Stefano Savino [b], Rafael López-Martín [a], Loreto Valenzuela [a,*]

[a] CIEMAT, Plataforma Solar de Almería, Tabernas, Almería, 04200, Spain
[b] Polytechnic Department of Engineering and Architecture, University of Udine, Udine, 33100, Italy

ARTICLE INFO

Keywords:
Parabolic trough collector
Receiver
Heat losses
Vacuum
Hydrogen permeation
Coupled heat transfer

ABSTRACT

This study investigates the thermal performance of linear evacuated receivers designed for parabolic trough collector (PTC) systems under varying operating conditions. A parametric thermal analysis was performed using ANSYS Fluent for a stainless steel receiver tube with Therminol® VP-1 as the heat transfer fluid. This fluid can produce low-boiling-point compounds, including hydrogen, which permeate through the absorber wall into the evacuated annulus between the absorber and the glass envelope of the receivers. Two annulus conditions were evaluated: a fully evacuated state (10^{-2} mbar) and hydrogen-filled environment (1 mbar). Additionally, the impact of wind speeds (5 and 10 m/s) on key performance parameters was assessed under two extreme operating conditions. Key metrics included temperature and velocity profiles, circumferential temperature gradients, convective heat transfer coefficients, and heat losses. Simulations covered mass flow rates of 3–6 kg/s (in 1 kg/s increments), inlet temperatures from 290 °C to 390 °C (in 20 °C steps), and direct normal irradiance levels of 800 and 1000 W/m^2. Results revealed how these annulus conditions and wind effects influence thermal performance. Hydrogen presence increased heat losses by up to 3 times compared to the evacuated case, with glass temperatures peaking at 142.5 °C. Increasing the mass flow rate from 3 to 6 kg/s reduced the absorber tube's maximum circumferential temperature difference from 39.4 °C to 23.5 °C, with different annulus conditions showing diminished impact on this parameter at higher flow rates. Heat losses increased under windy conditions, whereas the glass temperature decreased significantly, especially for the hydrogen-filled annulus.

1. Introduction

The growing adoption of parabolic trough collector (PTC) technologies in commercial solar thermal energy applications drives the need for accurate receiver modeling to optimize thermal efficiency and enhance operational reliability of this type of systems. The linear receiver of a PTC (commonly called absorber or heat collection element) [1,2] consists typically of a stainless steel tube enclosed within an anti-reflective borosilicate glass tube (also known as glass envelope or glass cover). Glass-to-metal seals are installed between the outer surface of the absorber and the glass tube to create a vacuum space in the annulus, reducing convective heat losses and preventing oxidative degradation of the steel tube's selective coating. Typically, the vacuum is maintained at 10^{-2} mbar. The selective coating helps to increase the absorptance of direct and reflected radiation and maintains a low thermal emissivity at high operating temperatures [3].

To enhance the performance of PTC solar thermal plants, heat losses in receiver tubes must be minimized. The thermal performance of PTC receivers was investigated in many studies. Forristall [4] developed a heat transfer model using Engineering Equation Solver (EES) to simulate the thermal behavior of PTC receivers, incorporating detailed thermodynamic and optical properties. Padilla et al. [5] conducted a one-dimensional numerical analysis of receiver heat transfer, validating their model with experimental data from Sandia National Laboratories. Kalogirou [6] presented a comprehensive thermal model that accounted for conduction, convection, and radiation losses, implemented in EES and validated against existing collector performance. Wu et al. [7] performed a three-dimensional transient simulation using CFD and Monte Carlo ray-tracing, revealing detailed temperature distributions and the impact of fluid velocity on thermal gradients. Guo et al. [8] investigated the influence of operating parameters on thermal and exergy efficiency, identifying optimal mass flow rates and highlighting the dominance of end losses.

In laboratory heat loss measurements, Burkholder et al. [9] tested commercial receivers under controlled conditions, showing that

* Corresponding author.
E-mail addresses: kumar.vinod@spes.uniud.it (V. Kumar), loreto.valenzuela@psa.es (L. Valenzuela).

https://doi.org/10.1016/j.applthermaleng.2026.129832
Received 24 May 2025; Received in revised form 16 October 2025; Accepted 13 January 2026
Available online 16 January 2026

Nomenclature

A_c	Flow cross-sectional area, m^2
A_{ri}	Receiver inner surface area, m^2
c_p	Specific heat, J/kg K
d_{gi}	Glass cover inner diameter, m
d_{go}	Glass cover outer diameter, m
d_{ri}	Receiver tube inner diameter, m
d_{ro}	Receiver tube outer diameter, m
ΔP	Pressure drop, Pa
f	Friction factor, –
g	Gravitational constant, m/s^2
h_{coef}	Heat transfer coefficient, W/m^2 K
L	Length, m
$\dot{m}$	Mass flow rate, kg/s
Nu	Nusselt number, –
Q_{cond}	Conduction heat loss, W/m
Q_{loss}	Total heat loss, W/m
Q_{rad}	Radiation heat loss, W/m
Q_{tot}	Total heat, W/m
Q_u	Useful heat, W/m
Ra	Rayleigh number, –
Re	Reynolds number, –
T_{amb}	Ambient temperature, °C
T_b	Bulk temperature, °C
T_{go}	Glass outer wall temperature, °C
T_{in}	Inlet temperature, °C
T_{out}	Outlet temperature, °C
T_{ri}	Receiver inner wall temperature, °C
T_{ro}	Receiver outer wall temperature, °C
T_{sky}	Sky temperature, °C
u_{in}	Inlet velocity, m/s
u_w	Wind speed, m/s

Greek Symbols

β	Thermal expansion coefficient, K^{-1}
ϵ	Emissivity, –
λ	Thermal conductivity, W/m K
μ	Dynamic viscosity, mPa s
ρ	Density, kg/m^3
$\sigma_{h,t}$	Turbulent Prandtl number, –

Subscripts

a	Air
amb	Ambient
avg	Average
f	HTF
g	Glass
gi	Glass inner
go	Glass outer
in	Inlet
max	Maximum
min	Minimum
r	Receiver
ri	Receiver inner
ro	Receiver outer

Abbreviation

DNI	Direct normal irradiance
HTF	Heat transfer fluid
LCR	Local concentration ratio
PSA	Plataforma Solar de Almería
PTC	Parabolic trough collector

hydrogen ingress significantly increases thermal losses. Burkholder and Kutscher [10] evaluated Solel's UVAC3 receiver, developing heat loss correlations based on absorber and ambient temperature differences. Lei et al. [11] introduced a new test stand and methodology to measure overall and end losses, demonstrating that end losses become more significant at lower operating temperatures. Marquez et al. [12] further contributed to the experimental characterization of receiver heat losses, focusing on the annulus region and resistance heating techniques.

The receiver is one of the most critical components of a PTC and is susceptible to performance degradation and damage. Over time, helium gas from the atmosphere could diffuse through the glass tube, increasing heat losses by up to 20% [13]. When vacuum is lost, the receiver experiences twice the normal heat loss. If the glass envelope is broken, the heat loss could be 4 to 10 times greater than that of an undamaged receiver, largely depending on wind conditions. Degradation of heat transfer fluids (HTFs) at high temperatures generates hydrogen gas, which slowly permeates through the absorber wall into the annular space, causing heat losses four times higher compared to those with a good vacuum [3,14,15]. Receiver failure rates were discussed in [16,17] to understand future trends, address operation and maintenance issues, and develop new designs with improved performance.

Over the past decade, extensive research has been conducted to enhance the performance of PTC systems, primarily by addressing heat losses that significantly impact efficiency and sustainability. Many studies have explored a wide range of factors, including geometrical design, receiver coatings, vacuum pressure, HTF flow and temperature, and ambient conditions such as wind velocity, to better understand and mitigate heat loss. A comprehensive literature review on heat losses in PTC receivers can be found in [18,19].

The thermal performance of a PTC is primarily affected by the heat transfer between the HTF and the absorber's inner wall, as well as between the absorber's outer wall and the glass envelope [20]. Burkholder and Kutscher [21] conducted laboratory heat loss tests on Schott's 2008 PTR70 parabolic trough receiver at receiver surface temperatures ranging from 100 °C to 500 °C. They observed that the receiver exhibited significantly lower heat losses compared to previous receiver designs, primarily due to improvements in the receiver's selective coating. At operating temperatures around 400 °C, the measured heat loss was approximately 190 W/m, representing a notable reduction compared to older receiver designs. Setien et al. [22] presented a methodology to analyze the influence of partial vacuum pressures in the heat losses of PTC receivers, considering air as an incoming gas. Utilizing infrared thermography, the approach enables noninvasive measurement of glass envelope temperatures, facilitating the detection of vacuum degradation. They measured a significant increase in glass cover temperature when the vacuum is completely lost (air pressure = 10^3 mbar) compared to when there is only a partial loss (10^{-4} mbar < air pressure < 10^2 mbar), regardless of the receiver temperature. Furthermore, several studies have used infrared thermography to evaluate the performance of receivers and detect faults in PTC fields. Caron and Röger [23] performed in-situ receiver heat-loss measurements through transient infrared thermography, providing valuable insights into local temperature variations and vacuum degradation. Carra et al. [24] investigated the influence of measurement parameters on vacuum level assessment in PTC receivers, improving the accuracy of thermographic diagnostics. Oufadel et al. [25] integrated infrared

imaging with artificial intelligence methods to estimate receiver heat losses in real operating conditions. This concept was further developed in [26] by applying a meta-learning framework with hypernetworks for efficient and scalable fault detection. Likewise, Price et al. [27] conducted an early field investigation to evaluate receiver performance and identify thermal anomalies under practical operating conditions.

Heat losses are directly proportional to the temperature of the glass. Under a given ambient condition, the glass temperature depends on the heat transfer mechanisms in the annulus. As vacuum pressure increases, conduction and natural convection heat transfer in the annulus also increase. Additionally, if gases with higher thermal conductivity than air – such as hydrogen, which has seven times the thermal conductivity of air – enter the annulus, they further enhance conduction and convection, resulting in an increased glass temperature. Hence, vacuum loss, by any means, can be detected using temperature sensors [28]. Glatzmaier [29] developed and tested a hydrogen measurement and extraction process at the Nevada Solar One (NSO) PTC solar power plant. An integrated sensor/separator system was installed to simultaneously measure hydrogen partial pressure and extract hydrogen from the headspace gas in the HTF expansion vessels. This system, based on a palladium/silver membrane design, allowed real-time monitoring of hydrogen levels without intrusive modifications to the plant. The technology was jointly developed by NREL and Acciona Energy and was then installed at full-scale at NSO. Lei et al. [30] numerically analyzed conduction and radiation heat losses in a PTC receiver using a 2-D heat transfer model applying the direct simulation Monte Carlo method and constant receiver tube temperature to predict heat loss for different residual gases at various annulus pressures and sizes. The results indicated that as the pressure increases, conductive heat transfer and total heat losses rise rapidly. Hydrogen and helium have a significant impact on conductive heat losses due to their thermodynamic properties. The emittance of the selective coating primarily affects radiation heat loss, while the gas species and annulus' pressure influence conductive heat loss.

Heat losses depend directly on absorber and glass tube temperatures, ambient and geometrical parameters, receiver emissivity, annulus vacuum pressure, and HTF inlet temperature, and indirectly on HTF mass flow rate [18,31]. Extensive research has been conducted on thermal performance under various conditions, and many studies have focused primarily on theoretical models or laboratory experiments using a constant receiver tube temperature without considering HTF flow rate or real operating conditions. In a PTC solar field, receiver tubes are subjected to non-uniform heat flux. Very few studies examine the thermal performance of receiver tubes under real operating conditions. Although previous studies have examined receiver heat losses, most have either treated the annulus region in isolation or assumed ideal conditions, ignoring the presence of hydrogen and the effects of outdoor winds. This study presents a detailed CFD-based thermal analysis of a PTC receiver of 70 mm absorber diameter, considering realistic scenarios involving a vacuum atmosphere at 10^{-2} mbar or hydrogen gas atmosphere at 1 mbar in the annulus space between the absorber and the glass tube, HTF mass flow rates ranging from 3 kg/s to 6 kg/s, inlet HTF temperatures between 290 °C and 390 °C, and direct normal irradiance (DNI) values of 800 W/m^2 and 1000 W/m^2. All baseline simulations were conducted under no-wind conditions to isolate the effects of internal flow and annulus properties. In a supplementary analysis, the influence of wind-induced forced convection on the external glass envelope was also investigated, considering wind speeds of 5 and 10 m/s to represent typical outdoor conditions. This addition provides insight into how external airflow modifies receiver heat losses and glass temperature, particularly under hydrogen-filled annulus conditions. By capturing the coupled effects of conduction, convection, and radiation heat transfer under these conditions, the model offers an accurate prediction of heat losses and thermal behavior of the receiver. The results not only deepen the understanding of thermal performance in degraded vacuum conditions but also provide practical insights for PTC field operators.

Table 1
Solar receiver tube model: main geometrical parameters and operating conditions.

Parameter & Value	
Inner diameter of the receiver tube, d_{ri} (m)	0.066
Outer diameter of the receiver tube, d_{ro} (m)	0.070
Inner diameter of the glass cover, d_{gi} (m)	0.114
Outer diameter of the glass cover, d_{go} (m)	0.120
Length, L (m)	4.06
Inlet HTF temperature, T_{in} (°C)	290, 310, 330, 350, 370, 390
Mass flow rate, $\dot{m}$ (kg/s)	3, 4, 5, 6
Direct normal irradiance, DNI (W/m^2)	800, 1000

2. Problem description

The study focuses on the analysis of a standard receiver tube designed for PTCs with a parabola aperture width of 5.76 m (LS-3 PTC design) [1]. This type of receiver has a cold length of 4060 mm and an outer absorber diameter of 70 mm. A schematic of a parabolic trough receiver is shown in Fig. 1, and detailed parameters of the receiver tube model are provided in Table 1.

Commercial PTC solar power plants widely use a eutectic mixture of biphenyl and diphenyl oxide as the heat transfer fluid due to the favorable thermodynamic properties of this synthetic thermal oil. The main materials relevant for the study and their thermophysical properties are discussed in the following subsection.

2.1. Material properties

2.1.1. Receiver

The absorber tube of commercial receivers for PTCs is generally made of stainless steel (grades 316 or 321), which is commonly used in PTC receivers due to its corrosion resistance, mechanical strength, durability, and excellent performance across a wide temperature range. Furthermore, it serves as a chemically and thermally stable substrate for the deposition of selective coatings, which are essential for enhancing the optical efficiency of these solar receivers. The temperature-dependent thermal conductivity of stainless steel λ_r can be evaluated as [32]:

$$\lambda_r = 0.0153 \cdot T_r + 14.775 \tag{1}$$

where T_r is the absorber tube temperature in K.

The outer surface of the absorber tube is coated with a material that has a temperature-dependent emissivity given by [32]:

$$\epsilon_{ro} = 0.062 + 2 \cdot 10^{-7} \cdot (T_{ro} - 273.15)^2 \tag{2}$$

The glass envelope surrounding the absorber tube is made of borosilicate glass, with a thermal conductivity λ_g of 1.2 W m^{-1} K^{-1} and an emissivity ϵ_g of 0.86.

2.1.2. Annulus material

To model the atmosphere in the annulus space between the absorber tube and the glass tube, two different scenarios are considered in the study: vacuum and low-pressure atmosphere with hydrogen. For hydrogen in the annular space, the density was based on the ideal gas law, and other properties were calculated using the kinetic theory model [33] provided by the CFD software used, i.e. ANSYS Fluent, to analyze conduction and natural convection effects.

2.1.3. Heat Transfer Fluid (HTF)

Therminol® VP-1 was used as the HTF circulating through the receiver tube, as it is widely used in the majority of operating CSP plants worldwide, with an installed capacity exceeding 4.5 to 5 GWe [34]. It is a commercially available eutectic mixture of diphenyl oxide and

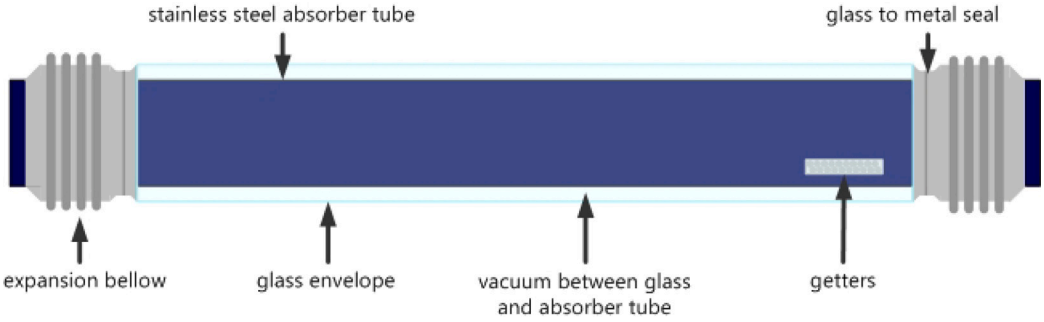

Fig. 1. Schematic of a solar receiver for a parabolic trough collector.

biphenyl, commonly employed in PTC solar power plants, and is marketed under several trade names, including Dowtherm® A, Therminol® VP-1, etc [35,36]. It operates effectively up to 400 °C [37].

Due to its low viscosity over the liquid-phase range, it enables efficient heat transfer. However, in environments where ambient temperatures drop below 12 °C, heat tracing is recommended to prevent solidification. The fluid remains thermally stable under normal operating conditions, but overheating may result in the formation of solid deposits on heating exchange surfaces. Additionally, degradation products – such as hydrogen and other low boilers – may accumulate in the vapor phase over time as the fluid ages, even under normal operating conditions. Therefore, proper circulation rates and control of pressure and temperature are essential. The temperature-dependent thermo-physical properties of Therminol® VP-1 are provided in the manufacturer's datasheets [38]. In this study, piecewise polynomials expressions are employed to model these properties for use in simulations and thermal analysis [32].

For the temperature range 285.15 K $\leq T \leq$ 698.15 K, the following expressions are considered for the specific heat capacity $c_{p,f}$ (in J kg^{-1} K^{-1}), density ρ_f (kg m^{-3}), and thermal conductivity λ_f (W m^{-1} K^{-1}) of the HTF:

$$c_{p,f} = 2.125 \cdot 10^3 - 11.017 \cdot T + 0.049862 \cdot T^2 - 7.7663 \cdot 10^{-5} \cdot T^3 + 4.394 \cdot 10^{-8} \cdot T^4 \quad (3)$$

$$\rho_f = 1.4386 \cdot 10^3 - 1.8711 \cdot T + 2.737 \cdot 10^{-3} \cdot T^2 - 2.3793 \cdot 10^{-6} \cdot T^3 \quad (4)$$

$$\lambda_f = 0.14644 + 2.0353 \cdot 10^{-5} \cdot T - 1.9367 \cdot 10^{-7} \cdot T^2 + 1.0614 \cdot 10^{-11} \cdot T^3 \quad (5)$$

Additionally, for the temperature range 373.15 K $\leq T \leq$ 698.15 K, the following expression is valid for the dynamic viscosity μ_f (mPa s) of the HTF:

$$\mu_f = 23.165 - 0.1476 \cdot T + 3.617 \cdot 10^{-4} \cdot T^2 - 3.9844 \cdot 10^{-7} \cdot T^3 + 1.6543 \cdot 10^{-10} \cdot T^4 \quad (6)$$

3. Numerical analysis

3.1. Governing equations and solution method

In this study, ANSYS Fluent 2025R1 [39] is used to solve the three-dimensional, steady-state Navier–Stokes equations for fully developed, incompressible turbulent flow in a smooth circular receiver tube of a PTC. Therminol® VP-1, with temperature-dependent thermophysical properties, is considered as the heat transfer fluid. Turbulence is modeled using the Shear Stress Transport (SST) k–ω model, which is widely used in engineering applications [40] and has been consistently applied in previous studies on similar systems [41,42].

The governing equations for the closed annulus between the absorber and the glass cover depend on the residual gas composition and pressure. In vacuum, heat transfer primarily occurs through radiation, as conduction and convection are negligible due to the absence of a medium for these modes of transfer. The degree of vacuum, or the pressure, directly impacts the amount of residual gas, affecting the possibility of conduction and convection. As pressure decreases, convection decreases, and at very low pressures, conduction also becomes negligible. In this study, two annulus atmosphere conditions are analyzed: (i) a low-pressure vacuum (10^{-2} mbar), and (ii) a hydrogen-filled annulus at 1 mbar. In ANSYS Fluent, these conditions are modeled accordingly. For the 10^{-2} mbar case, conduction is simulated by solving only the energy equation in the domain, with flow variables disabled; while for the 1 mbar hydrogen case, as the Rayleigh numbers is less than 1.0×10^8, it is appropriate to model the buoyancy-induced flow as laminar within the closed annular region [43], with the turbulence model disabled in this specific domain. Under the operating conditions of this study the Knudsen number, calculated using a representative physical length corresponding to the thickness of the annular gap, is of the order of 10^{-3}, thus validating the continuum hypothesis.

The Surface-to-Surface (S2S) radiation model is employed to evaluate radiative heat transfer between the outer surface of the receiver tube and the inner surface of the glass cover [20,43,44].

The continuity, momentum and energy equations for the fluid domains are given by Eqs. (7)–(9) [42,45],

$$\frac{\partial(\rho u_i)}{\partial x_i} = 0 \quad (7)$$

$$\frac{\partial}{\partial x_j}\left(\rho u_i u_j\right) = \rho g_i - \frac{\partial p}{\partial x_i} + \frac{\partial}{\partial x_j}\left\{\left(\mu + \mu_t\right)\left(\frac{\partial u_i}{\partial x_j} + \frac{\partial u_j}{\partial x_i}\right) - \frac{2}{3}\left[\left(\mu + \mu_t\right)\frac{\partial u_k}{\partial x_k} + \rho k\right]\delta_{ij}\right\} \quad (8)$$

$$\frac{\partial}{\partial x_j}\left(\rho c_p u_j T\right) = \frac{\partial}{\partial x_j}\left[\left(\lambda + c_p\frac{\mu_t}{\sigma_{h,t}}\right)\frac{\partial T}{\partial x_j}\right] \quad (9)$$

In the continuity and momentum equations, u_i and u_j are time-averaged velocity components, p is the time-averaged pressure, μ_t is the turbulent viscosity, ρg_i denotes the gravitational body force components, and k is the turbulent kinetic energy. In the energy equation, T is the time-averaged temperature, and $\sigma_{h,t}$ is the turbulent Prandtl number.

Turbulent kinetic energy k and the turbulent energy dissipation ω are given as [41,42,45],

$$\frac{\partial(\rho k)}{\partial t} + \frac{\partial(\rho k u_i)}{\partial x_i} = \frac{\partial}{\partial x_j}\left(\Gamma_k\frac{\partial k}{\partial x_j}\right) + G_k - Y_k + G_b \quad (10)$$

$$\frac{\partial(\rho \omega)}{\partial t} + \frac{\partial(\rho \omega u_i)}{\partial x_i} = \frac{\partial}{\partial x_j}\left(\Gamma_\omega\frac{\partial \omega}{\partial x_j}\right) + G_\omega - Y_\omega + G_{\omega b} \quad (11)$$

where G_k is the production of turbulent kinetic energy due to mean velocity gradients, G_ω is the production of ω, Γ_k and Γ_ω are the effective diffusivities of k and ω, Y_k and Y_ω represent their dissipation due to turbulence, and G_b and $G_{\omega b}$ represent the buoyancy terms.

The energy equation for the solid domains is given by Eq. (12) [45]

$$\frac{\partial}{\partial x_j}\left(\lambda\frac{\partial T}{\partial x_j}\right) = 0 \quad (12)$$

In the above equations, the thermophysical properties, namely ρ, c_p, μ, and λ, are those pertaining to the appropriate domain where the equations are solved. For the fluid domains (i.e. HTF and Annulus as shown in Fig. 2(a)), these are the properties of the heat transfer fluid and the hydrogen, while for the solid domains (i.e. Receiver tube and Glass cover as shown in Fig. 2(a)), these are the properties of the stainless steel and the borosilicate glass. In the annular region, where the flow is laminar, all turbulent terms in Eqs. (8)–(9) are omitted.

A coupled algorithm is used for pressure–velocity coupling, while a second-order upwind scheme is applied for the discretization of the governing equations. Numerical simulations are performed until the residuals for all solution variables fall below $1 \cdot 10^{-6}$.

3.2. Boundary conditions

The simulation model's boundary conditions are defined as follows:

- Inlet and outlet of the HTF in the receiver
  - Inlet: Constant mass flow rate ($\dot{m}$) and temperature (T_{in}).
  - Outlet: Pressure outlet boundary condition was specified.

  Four mass flow values (3, 4, 5, and 6 kg/s) and inlet temperatures ranging from 290 °C to 390 °C (in 20 °C increments) are analyzed.
- Absorber tube walls
  - Inner wall: Coupled thermal boundary condition (no-slip velocity, conjugated heat transfer between fluid and solid zones).
  - Outer wall: Coupled thermal boundary condition. The non-uniform heat flux (LS-3 profile, see Fig. 2(b) for a qualitative distribution) is applied via ANSYS Fluent's Thin-Wall model using a user-defined expression (UDE) [39]. The heat flux is expressed as the product of the direct normal irradiance (DNI) and a function of the local concentration ratio (LCR) [46], as illustrated in Fig. 2(c). Two DNI values are used: 850 W/m^2 and 1000 W/m^2. The LCR distribution was adopted from the optical simulation of the LS-3 collector performed by Wang et al. [46], who used a Monte Carlo Ray Tracing (MCRT) model validated for the DISS project. Their model accounted for mirror reflectance (≈0.94), glass transmittance (≈0.96), and absorber absorptance (≈0.96), reproducing the realistic non-uniform flux distribution along the receiver circumference. In this study, the normalized LCR profile from that work was directly imposed through the relation

    $$q''(\theta) = \mathrm{LCR}(\theta) \times \mathrm{DNI} \tag{13}$$

    which provides a physically consistent and computationally efficient representation of the LS-3 flux pattern.
    The radiative exchange with the glass cover inner wall is accounted for by the Surface to Surface model (S2S) [20]. The emissivity of the receiver's outer wall coating, denoted as ϵ_{ro}, is expressed as a temperature-dependent function of the outer surface temperature, as shown in Eq. (2).
- Annulus and solid Domain ends
  - Adiabatic walls (zero heat flux) at both ends of the annulus, absorber tube material, and glass cover.
- Glass cover walls
  - Inner wall: Coupled thermal boundary condition. The radiative exchange with the receiver outer wall is accounted for by the Surface to Surface model (S2S).
  - Outer wall: Mixed convection-radiation boundary condition. The emissivity of the glass cover ϵ_g is 0.86, the ambient temperature T_{amb} is 25 °C, and the sky temperature T_{sky} is 17 °C. In this study, both the no-wind (natural convection) case and the effect of wind (forced convection) around the glass cover are considered. The following correlations are used: natural convection (without wind) h_w [47] and forced convection (with wind) h_f [20].

    $$h_w = \left(0.48\,\mathrm{Ra}_{d_{go}}^{0.25}\right)\frac{\lambda_a}{d_{go}} \tag{14}$$

    where λ_a is the air thermal conductivity at ambient temperature and $\mathrm{Ra}_{d_{go}}$ is the Rayleigh number for air based on the glass cover outer diameter and calculated as

    $$\mathrm{Ra}_{d_{go}} = g\beta_a \Delta T \frac{d_{go}^3 \rho^2 c_{p,a}}{\mu_a \lambda_a} \tag{15}$$

    where β_a is the thermal expansion coefficient, ΔT is the temperature difference between the ambient temperature T_{amb} and the glass cover temperature T_{go}, and ρ_a, $c_{p,a}$, μ_a are the air thermal properties at ambient temperature.

    $$h_f = 4\,u_w^{0.58}\,d_{go}^{-0.42} \tag{16}$$

    where u_w is wind speed.

3.3. Post-processing of numerical data

To extract meaningful physical insights from the CFD simulations, key dimensionless numbers are calculated. These quantities allow for the comparison of numerical results with predictions and experimental data, and facilitate the validation of the simulation approach. The following parameters are evaluated. The Reynolds number, Re, is calculated as,

$$\mathrm{Re} = \frac{4\,\dot{m}}{\pi\, d_{ri}\, \mu_f} \tag{17}$$

The Darcy friction factor, f, is determined by

$$f = \frac{\Delta P\, d_{ri}/L}{\rho_f\, u_{in}^2/2} \tag{18}$$

where ΔP is the pressure drop, L is the receiver length, ρ_f is the HTF density, and u_{in} is the inlet velocity in the z-direction, and is calculated as

$$u_{in} = \frac{\dot{m}}{\rho_f\, A_c} \tag{19}$$

with A_c being the absorber tube cross-sectional area.

The maximum circumferential temperature difference at the absorber outer wall, ΔT_{max}, is calculated as

$$\Delta T_{max} = T_{ro,max} - T_{ro,min} \tag{20}$$

where $T_{\mathrm{ro,\,max}}$ and $T_{\mathrm{ro,\,min}}$ are the maximum and minimum outer wall temperatures, respectively.

The convective heat transfer coefficient of the HTF, h_{coef}, is obtained from

$$h_{\mathrm{coef}} = \frac{Q_u}{A_{ri}\left(T_{ri} - T_b\right)} \tag{21}$$

where Q_u is the useful heat absorbed by the HTF, A_{ri} is the absorber inner surface area, T_{ri} is the absorber inner wall temperature, and T_b is the bulk temperature of the HTF.

The average Nusselt number, Nu, is then calculated as,

$$\mathrm{Nu} = \frac{h_{\mathrm{coef}}\, D_{ri}}{\lambda_f} \tag{22}$$

where λ_f is the thermal conductivity of the HTF.

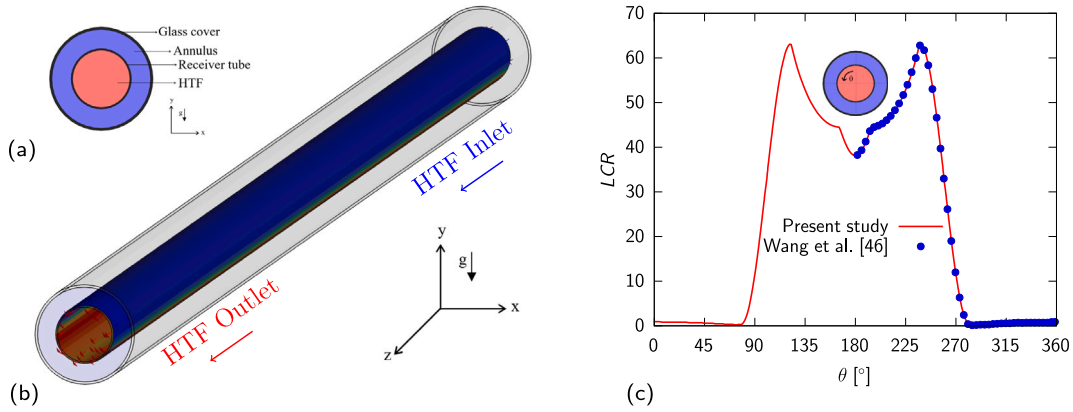

Fig. 2. (a) Cross section of a receiver tube, (b) receiver tube with qualitative heat flux distribution, and (c) LCR profile.

Total heat loss, Q_{loss}, is determined by

$$Q_{loss} = Q_{tot} - Q_u = Q_{rad} + Q_{cond} \tag{23}$$

where Q_{tot} is the total heat input at receiver outer surface, and Q_{rad} and Q_{cond} are the radiative and conductive heat losses, respectively.

To validate the numerical results, the friction factor and Nusselt number were also calculated using the Petukhov and Gnielinski correlations, respectively, which are widely accepted for turbulent flow in smooth tubes:

- Petukhov correlation [48]

$$f = (0.790 \ln \mathrm{Re} - 1.64)^{-2} \tag{24}$$

- Gnielinski correlation [49]

$$\mathrm{Nu} = \frac{\left(\frac{f}{8}\right)(\mathrm{Re} - 1000)\,\mathrm{Pr}}{1 + 12.7\left(\frac{f}{8}\right)^{0.5}\left(\mathrm{Pr}^{\frac{2}{3}} - 1\right)} \tag{25}$$

where Pr is the Prandtl number.

4. Grid independence analysis and model validation

4.1. Grid independence analysis

To ensure numerical accuracy, five hexahedral meshes with increasing refinement (coarse, with 895,230 elements, to fine, with 3,093,000 elements), were generated using the ANSYS Meshing tool. The meshes were evaluated at one of the operational conditions: inlet temperature T_{in} = 390 °C and maximum mass flow rate $\dot{m}$ = 6 kg/s. The height of the first element on the inner wall of the HTF domain was kept constant across all meshes at 9.8 μm. For the maximum flow rate investigated, this ensured maximum and average dimensionless wall distances y^+ of 3.4 and 2.3, respectively, both consistent with the adopted turbulence model. As shown in Fig. 3(a), both key global output parameters (e.g., pressure drop ΔP and average temperature on the outer glass surface $T_{go,avg}$) and a local parameter (e.g., maximum temperature on the outer receiver surface $T_{ro,max}$) showed negligible variation beyond Mesh 4. The maximum temperature on the external surface of the glass was also monitored to assess mesh adequacy for estimating radiative exchange. Similar monotonic behaviors, like those shown in Fig. 3 and not reported here for brevity, were observed for other global and local parameters, such as HTF outer temperature, average temperature on the outer receiver surface, and maximum outer glass surface temperature, with variations between Mesh 4 and Mesh 5 smaller than 0.08%. Consequently, Mesh 4, which contains 2.61 million elements, was selected as the optimal balance between computational cost and result accuracy. A detailed cross-sectional view of Mesh 4 is provided in Fig. 3(b). In the final mesh, the growth rate in the HTF region between the wall and the channel core, where a uniform size mesh was applied, was set to a low value of 1.08 to capture flow structures even away from the wall accurately.

Subsequent validation of the Mesh 4 results against experimental and analytical data is presented in Section 4.2.

4.2. Numerical model validation

The numerical results of the developed parabolic trough receiver model were validated using both empirical correlations and experimental data. First, the pressure drop, expressed in terms of the friction factor, was validated using the Petukhov correlation [48], as shown in Fig. 4(a). Similarly, the heat transfer coefficient, characterized by the Nusselt number, was validated using the Gnielinski correlation [49], as shown in Fig. 4(b). The mean deviations were 0.96% for the friction factor and 1.4% for the Nusselt number, both of which are low values that further confirm the validity and reliability of the developed model.

Subsequently, the CFD model results were further validated by comparison with laboratory experimental data obtained at the Plataforma Solar de Almería (PSA)-CIEMAT and the National Renewable Energy Laboratory (NREL) [21]. Heat loss (Q_{loss}) and glass cover temperature (T_{go}) were validated under vacuum conditions, as shown in Fig. 5. As can be seen, the numerical results closely match the experimental data. The mean deviations were 5.5% for heat loss and 3.1% for glass temperature, both of which are low values that further confirm the validity and reliability of the developed model.

In addition to the vacuum condition, the CFD model was also validated for cases with hydrogen present in the annulus. Experimental data from the Plataforma Solar de Almería (PSA) [50] and the Forristall EES model [4] were used for comparison. Fig. 6 shows the variation of heat loss (Q_{loss}) and glass cover temperature (T_{go}) with receiver inner wall temperature under hydrogen conditions. The mean deviation for heat loss was 11.2% with respect to the PSA data and 9.7% with respect to the Forristall model. For the glass temperature, the mean deviation was 15.5% with respect to the PSA data and 6.7% with respect to the Forristall model. These results confirm that the developed CFD model provides a reliable prediction of the receiver's thermal performance even under non-vacuum (hydrogen) conditions.

It is worth noting that the slightly higher deviation observed for the hydrogen-filled annulus compared to the vacuum case can be attributed to the complex and dynamic behavior of hydrogen within the annulus. Unlike vacuum conditions, where heat transfer is dominated by radiation, the presence of hydrogen introduces additional convective and conductive heat transfer mechanisms that are highly sensitive to local pressure, temperature, and gas composition. Furthermore, unsteady hydrogen flow within the glass envelope may occur due to the gradual release or re-absorption of hydrogen by the getter materials, which are affected by the instantaneous getter temperature and hydrogen

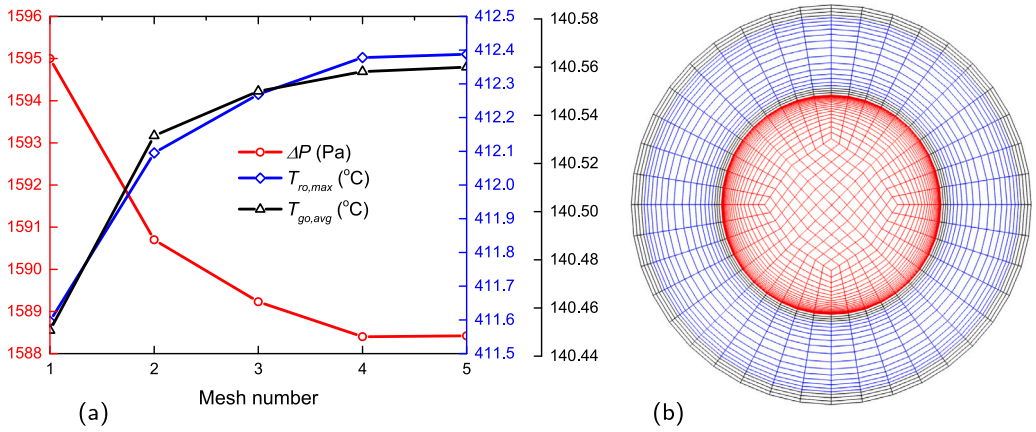

Fig. 3. (a) Grid independence test results; (b) cross-sectional detail of the final mesh for the receiver.

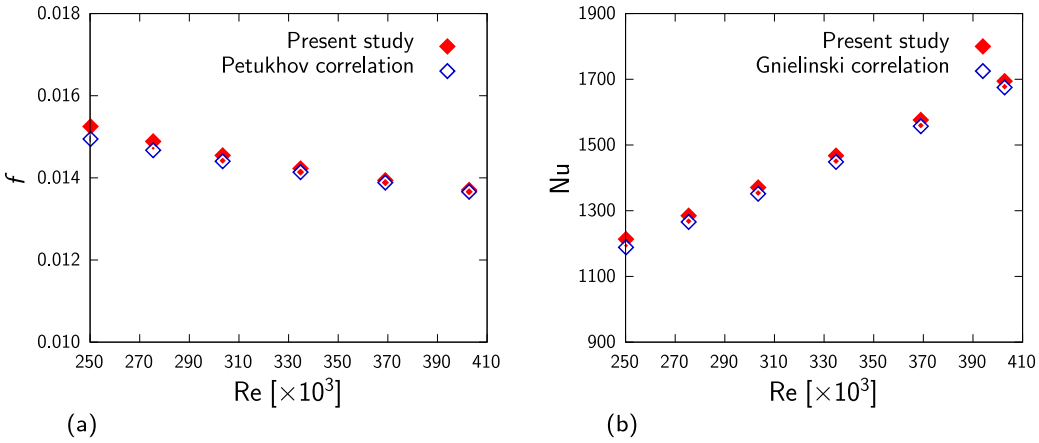

Fig. 4. Validation of CFD numerical results compared to correlation results : (a) friction factor, and (b) Nusselt number.

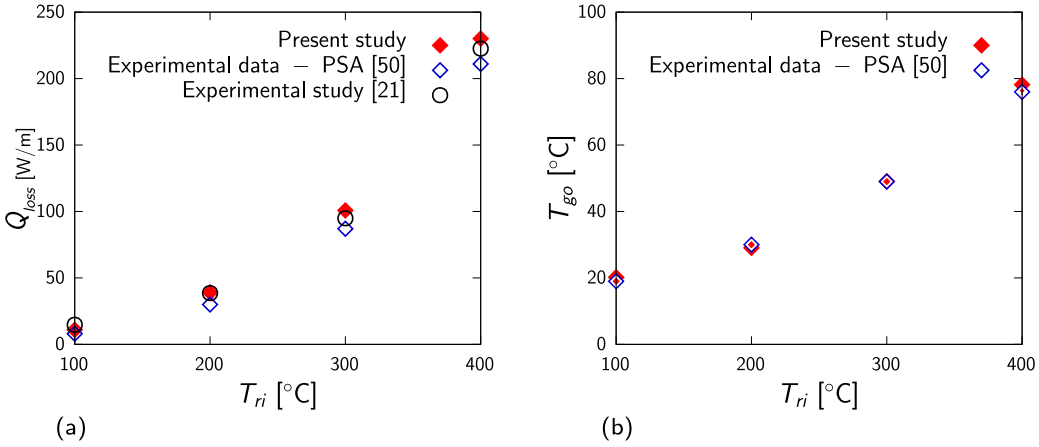

Fig. 5. Validation of CFD numerical results compared to experimental data under vacuum condition: (a) heat loss, and (b) glass cover temperature.

pressure. These factors make it more challenging to reach a steady-state condition experimentally, contributing to the observed discrepancies. Despite these complexities, the CFD model successfully reproduces the overall heat-loss trends, demonstrating good predictive capability under hydrogen-filled operating conditions.

5. Results and discussion

The numerical results are presented and discussed below. First, the fluid temperature inside the absorber tube, velocity contours, and velocity vectors are shown for two cases: with vacuum in the annular space and with hydrogen, under the defined operating conditions. For clarity, only specific regions of the domain, typically the HTF or vacuum zone, are shown separately in the qualitative figures of Sections 5.1 and 5.2. This approach is taken because temperature and velocity ranges differ significantly across the domain, making a unified representation difficult to interpret. Next, the temperature profiles of the absorber and glass tubes are presented. Finally, the heat losses for both conditions of the receiver tube – vacuum and hydrogen in the annulus – are discussed.

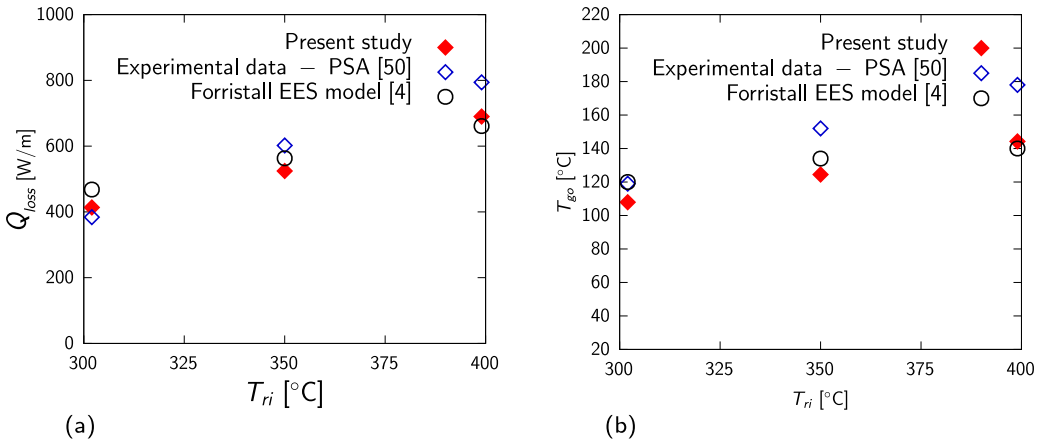

Fig. 6. Validation of CFD numerical results compared to experimental data under hydrogen condition: (a) heat loss, and (b) glass cover temperature.

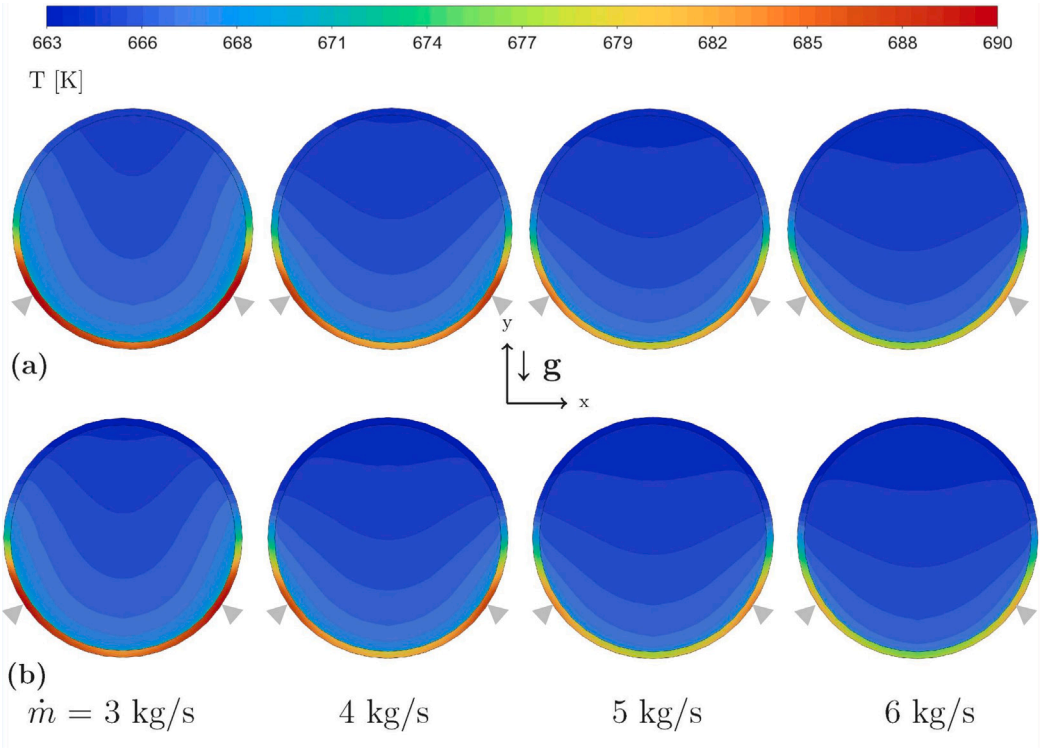

Fig. 7. Temperature contours at the outlet of the absorber tube for T_{in} = 390 °C and DNI = 850 W/m^2: (a) vacuum in the annulus; (b) hydrogen in the annulus. Light gray arrows indicate the locations of heat-flux peaks.

5.1. Temperature, velocity contours, and velocity vectors

Fig. 7 shows the temperature contours at the outlet of the absorber tube for an inlet temperature (T_{in}) of 390 °C and direct normal irradiance (DNI) of 850 W/m^2, at mass flow rates of 3, 4, 5, and 6 kg/s. Fig. 7a and b show the temperature profiles for vacuum and for hydrogen in the annulus, respectively. As the mass flow rate increases, the circumferential temperature decreases; however, so does the outlet HTF temperature. As can be seen, the maximum temperatures in the receiver tube occur at locations corresponding to the peak heat-flux values, which are indicated in the figure by light gray arrows. As shown in Fig. 7b, the presence of hydrogen in the annulus (due to its high thermal conductivity) originates greater conductive and convective heat loss, resulting in a slightly cooler absorber tube surface compared to the vacuum case.

The velocity contours at the outlet of the absorber tube for T_{in} = 390 °C and DNI = 850 W/m^2 are shown in Fig. 8, for mass flow rates of 3, 4, 5, and 6 kg/s. Only the results for hydrogen in the annulus are presented, as internal fluid flow in the absorber tube (represented by the velocity contours) is almost identical for both the vacuum and hydrogen annulus conditions.

This study analyzed only one position of the receiver tube, with the concentrated heat flux impinging on the receiver from below (the parabola facing the zenith). The direction of gravity is also indicated in the figures. In addition to forced convection, natural convection arises due to the temperature-dependent properties of the HTF. At lower mass flow rates, the fluid velocity is reduced, and the maximum velocity (indicated by a white cross symbol) is observed away from the center of the tube, as shown in Fig. 8. This behavior is attributed to the combined influence of natural convection effects and weaker turbulent forces on the velocity profile. As the mass flow rate increases, turbulent forces become more dominant, causing the location of the maximum velocity to shift towards the center of the tube.

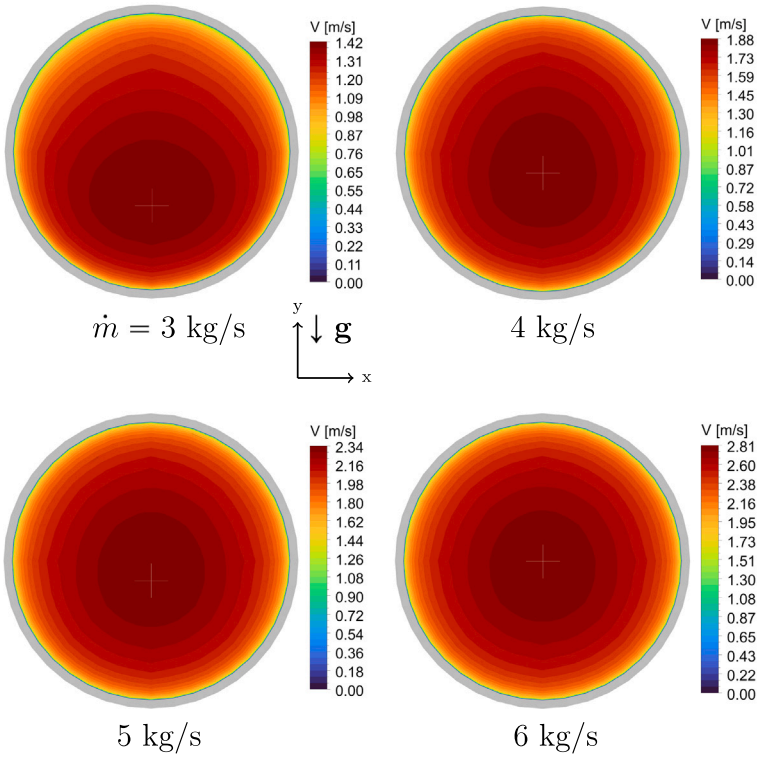

Fig. 8. Velocity contours at the outlet of the absorber tube for T_{in} = 390 °C and DNI = 850 W/m^2.

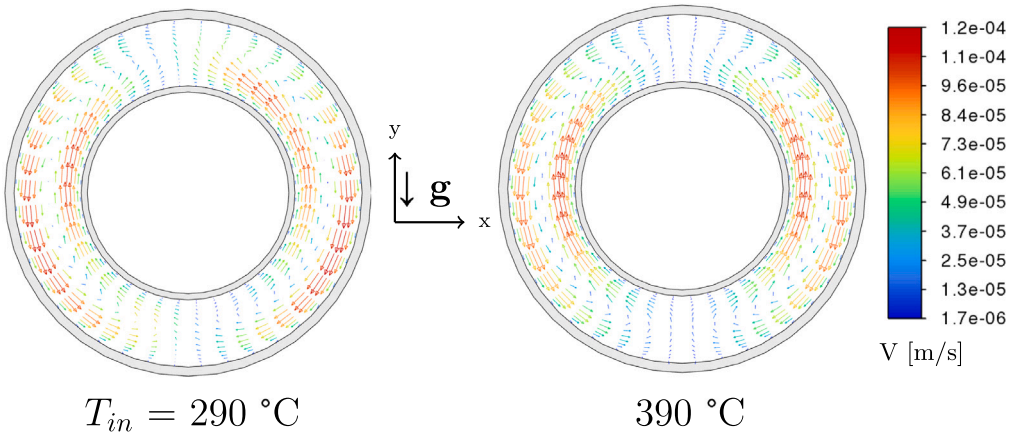

Fig. 9. Velocity vectors in the annulus space filled with hydrogen at a pressure of 1 mbar (cross-section at the end of the receiver tube), with $\dot{m}$ = 3 kg/s and DNI = 850 W/m^2.

Fig. 9 shows the velocity vectors of hydrogen in the closed annulus between the outer surface of the absorber tube and the inner surface of the glass envelope, at both lower and higher inlet temperatures of the HTF, for $\dot{m}$ = 3 kg/s and DNI = 850 W/m^2 in the x-y plane. The flow pattern in the annular space appears mostly symmetric, with one vortex rotating counterclockwise on the left and another rotating clockwise on the right. This buoyancy-driven flow occurs because the outer surface of the absorber tube is hot while the inner surface of the glass envelope is cold. As a result, hydrogen rises along the hot outer surface and descends along the cold inner surface. As expected, the natural convection is more intense for the higher HTF inlet temperature T_{in}.

5.2. Temperature profile of absorber and glass envelope outer surfaces

Fig. 10 presents the circumferential temperature distribution on the right half of the absorber surface (180° ≤ θ ≤ 360°) and the corresponding outer surface of the glass tube at T_{in} = 390 °C and DNI = 850 W/m^2, for annulus conditions of vacuum (10^{-2} mbar) and hydrogen (1 mbar) at z = 3.86 m, i.e. a cross-section close to the receiver outlet. Under vacuum, the absorber surface maintains slightly higher temperatures due to negligible convective heat losses, while the presence of hydrogen slightly reduces the surface temperature due to higher conductive and convective heat transfer. On the glass tube side, hydrogen raises the outer surface temperature to approximately 142 °C, compared to 74°C under vacuum, as a result of increased heat transfer via conduction and convection. This increase in the glass envelope temperature in the presence of hydrogen not only increases heat loss but may also induce high stresses in the glass-to-metal seals of the receiver tube, which could ultimately lead to receiver failure. The average outer surface temperatures of the absorber and glass tubes at varying inlet HTF temperatures and mass flow rates, for both vacuum and hydrogen annulus conditions, are presented in Table A.6 (see Appendix A).

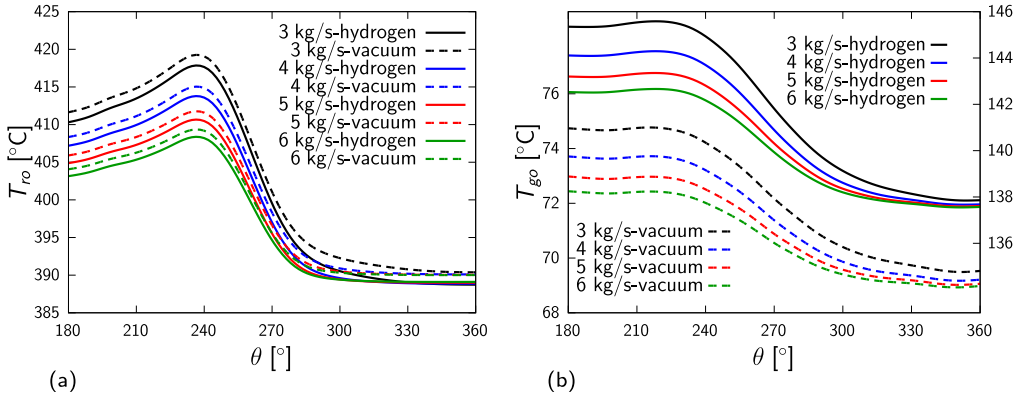

Fig. 10. Temperature profiles on the outer surfaces of the absorber tube (a) and glass envelope (b) at T_{in} = 390°C and DNI = 850 W/m^2.

Table 2
Maximum circumferential temperature differences in the absorber tube.

$\dot{m}$	T_{in}	Vacuum		Hydrogen	
(kg/s)	(°C)	850 (W/m^2)	1000 (W/m^2)	850 (W/m^2)	1000 (W/m^2)
		ΔT_{max} (°C)	ΔT_{max} (°C)	ΔT_{max} (°C)	ΔT_{max} (°C)
3	290	33.7	39.4	33.4	39.1
	310	33.0	38.6	32.8	38.3
	330	32.3	37.8	32.1	37.5
	350	31.7	37.0	31.5	36.8
	370	31.1	36.3	31.0	36.2
	390	30.7	35.9	30.6	35.7
4	290	28.6	33.5	28.3	33.2
	310	27.9	32.8	27.7	32.5
	330	27.3	32.1	27.2	31.9
	350	26.8	31.4	26.6	31.2
	370	26.3	30.8	26.1	30.7
	390	25.9	30.4	25.7	30.2
5	290	24.9	29.2	24.7	29.0
	310	24.3	28.6	24.1	28.3
	330	23.8	27.9	23.6	27.7
	350	23.3	27.3	23.1	27.1
	370	22.8	26.8	22.6	26.6
	390	22.4	26.4	22.3	26.2
6	290	22.2	26.0	22.0	25.8
	310	21.6	25.5	21.5	25.3
	330	21.2	24.9	21.0	24.7
	350	20.7	24.4	20.6	24.2
	370	20.3	23.9	20.2	23.7
	390	20.0	23.5	19.8	23.3

Table 3
Convective heat transfer coefficient (h_{coef}).

$\dot{m}$	T_{in}	Vacuum		Hydrogen	
(kg/s)	(°C)	850 (W/m^2)	1000 (W/m^2)	850 (W/m^2)	1000 (W/m^2)
		h_{coef} (W/m^2 K)	h_{coef} (W/m^2 K)	h_{coef} (W/m^2 K)	h_{coef} (W/m^2 K)
3	290	1848.3	1856.8	1847.6	1856.3
	310	1888.4	1897.1	1887.7	1896.6
	330	1928.8	1937.8	1928.1	1937.2
	350	1969.2	1978.1	1968.4	1977.6
	370	2006.0	2014.6	2005.2	2014.1
	390	2030.9	2038.4	2030.0	2037.9
4	290	2299.8	2304.5	2299.2	2304.0
	310	2354.3	2358.9	2353.7	2358.3
	330	2408.9	2413.5	2408.3	2412.9
	350	2463.5	2468.0	2462.8	2467.3
	370	2514.0	2517.9	2513.3	2517.1
	390	2550.3	2552.7	2549.4	2551.9
5	290	2755.1	2758.1	2754.8	2757.8
	310	2824.1	2826.9	2823.7	2826.5
	330	2893.0	2895.6	2892.6	2895.2
	350	2961.8	2964.1	2961.4	2963.7
	370	3025.9	3027.4	3025.4	3027.0
	390	3073.4	3073.4	3072.9	3073.0
6	290	3206.2	3208.6	3206.1	3208.4
	310	3289.2	3291.2	3289.0	3291.1
	330	3371.8	3373.6	3371.6	3373.4
	350	3454.2	3455.7	3454.1	3455.5
	370	3531.4	3532.1	3531.2	3531.9
	390	3589.7	3588.9	3589.5	3588.7

5.3. Maximum circumferential temperature difference on the absorber tube surface (ΔT_{max})

Due to the non-uniform heat flux distribution on the absorber tube, circumferential temperature variations occur along the absorber's periphery. Under normal operating conditions, the maximum allowable temperature difference across the cross-section of the tube should not exceed 50 °C approximately [46].

A low mass flow rate of HTF significantly increases the circumferential temperature difference, leading to potential absorber tube deflection or other failures. Therefore, controlling circumferential temperature gradients of the absorber tube surface is essential in the design and evaluation of a receiver. Table 2 presents the circumferential temperature differences, ΔT_{max}, in a receiver tube under vacuum and hydrogen annulus conditions for various mass flow rates, inlet temperatures, and DNI values (850 and 1000 W/m^2). The results indicate, as expected, that ΔT_{max} decreases with increasing mass flow rate and inlet temperature. For example, at 3 kg/s and T_{in} = 290 °C, the maximum ΔT_{max} reaches 39.4 °C, with vacuum, and 39.1 °C, with hydrogen, at DNI = 1000 W/m^2. However, at 6 kg/s, ΔT_{max} drops to 23.5 °C and 23.3 °C, respectively, highlighting the effectiveness of this higher flow rate in increasing the heat transfer rate in the absorber tube wall and, then, in minimizing thermal gradients. These mass flow rates, as mentioned before, represent working conditions that are typically set in the operation of solar power plants with PTCs and thermal oil as HTF.

The convective heat transfer coefficient, h_{coef}, at the inner wall of the absorber tube, as shown in Table 3, shows a clear increasing trend with both mass flow rate and inlet temperature across all tested conditions. At a constant direct normal irradiance (DNI), increasing the flow rate from 3 to 6 kg/s results in a significant rise in h_{coef}. For instance, at T_{in} = 290 °C and DNI = 850 W/(m^2 K), h_{coef} increases from 1848.3 to 3206.2 W/(m^2 K). Similarly, at a fixed flow rate (e.g., 5 kg/s), raising the inlet temperature from 290 °C to 390 °C increases h_{coef} from 2755.1 to 3073.4 W/(m^2 K). This enhancement is attributed to improved convective heat transfer resulting from higher Reynolds numbers and reduced viscosity of Therminol® VP-1 at elevated temperatures. Additionally, the difference in h_{coef} between vacuum (10^{-2} mbar) and hydrogen (1 mbar) annulus conditions remains negligible (typically < 1 W/(m^2 K)) across all scenarios, indicating that internal convection dominates heat transfer within the absorber tube.

Table 4
Total heat loss (Q_{loss}) and radiation heat loss (Q_{rad}).

$\dot{m}$	T_{in}	Vacuum		Hydrogen		H_2/Vac	Vacuum		Hydrogen		H_2/Vac
(kg/s)	(°C)	Q_{loss} (W/m)		Q_{loss} (W/m)			Q_{rad} (W/m)		Q_{rad} (W/m)		
		850 (W/m^2)	1000 (W/m^2)	850 (W/m^2)	1000 (W/m^2)	1000 (W/m^2)	850 (W/m^2)	1000 (W/m^2)	850 (W/m^2)	1000 (W/m^2)	1000 (W/m^2)
3	290	100.3	102.7	442.6	449.7	4.38	100.3	102.6	88.5	90.9	0.886
	310	119.2	121.8	489.9	497.4	4.08	119.1	121.7	105.7	108.4	0.891
	330	140.8	143.8	540.4	548.3	3.81	140.7	143.7	125.5	128.6	0.895
	350	165.7	169.0	594.3	602.6	3.57	165.5	168.8	148.3	151.8	0.899
	370	194.2	197.9	651.9	660.7	3.34	193.9	197.6	174.5	178.4	0.903
	390	226.7	230.9	713.8	723.2	3.13	226.4	230.6	204.5	208.9	0.906
4	290	98.0	99.9	437.1	443.2	4.44	98.0	99.9	86.6	88.6	0.887
	310	116.6	118.7	484.2	490.6	4.13	116.5	118.6	103.5	105.8	0.892
	330	137.9	140.4	534.5	541.2	3.86	137.8	140.2	123.1	125.6	0.896
	350	162.5	165.2	588.2	595.3	3.60	162.2	165.0	145.6	148.5	0.900
	370	190.5	193.6	645.6	653.1	3.37	190.3	193.3	171.5	174.7	0.904
	390	222.7	226.1	707.2	715.2	3.16	222.3	225.7	201.2	204.8	0.907
5	290	96.5	98.1	433.5	438.8	4.47	96.5	98.1	85.3	87.0	0.887
	310	114.9	116.7	480.5	486.1	4.17	114.8	116.6	102.1	104.0	0.892
	330	136.0	138.1	530.6	536.5	3.89	135.9	137.9	121.5	123.7	0.897
	350	160.3	162.6	584.1	590.4	3.63	160.1	162.4	143.8	146.3	0.901
	370	188.2	190.8	641.4	648.0	3.40	187.9	190.5	169.5	172.3	0.904
	390	220.1	222.9	702.8	709.9	3.19	219.7	222.6	199.0	202.1	0.908
6	290	95.4	96.9	430.9	435.7	4.50	95.4	96.8	84.4	85.9	0.887
	310	113.7	115.3	477.8	482.9	4.19	113.6	115.2	101.1	102.8	0.892
	330	134.7	136.5	527.9	533.2	3.91	134.5	136.3	120.4	122.3	0.897
	350	158.9	160.9	581.3	587.0	3.65	158.6	160.6	142.6	144.8	0.902
	370	186.6	188.8	638.5	644.5	3.41	186.2	188.5	168.1	170.6	0.905
	390	218.2	220.8	699.8	706.2	3.20	217.8	220.3	197.5	200.3	0.909

5.4. Heat losses

A significant difference in thermal behavior is observed between vacuum and hydrogen annulus conditions, primarily due to the presence (hydrogen) or absence (vacuum) of convective heat transfer in the annulus space between the absorber tube and the glass envelope. Heat losses for both cases, provided in Table 4 together with the ratio H_2/Vac between hydrogen and vacuum conditions results, highlight this distinction.

Under vacuum annulus condition, heat losses are significantly lower due elimination of convection, leaving radiation as the dominant loss mechanism. In contrast, introducing hydrogen at 1 mbar enables convective heat transfer, substantially increasing total heat losses. For example, at a mass flow rate of 3 kg/s, an inlet temperature of T_{in} = 390 °C, and DNI = 1000 W/m^2, total heat loss rises from 230.9 W/m (vacuum) to 723.2 W/m (hydrogen), highlighting the critical need to maintain high-vacuum conditions.

Heat losses also increase with inlet temperature across all cases due to higher absorber surface temperatures. Under vacuum, radiation dominates, as evidenced by the rise in Q_{loss} from 100.3 W/m at 290 °C to 226.7 W/m at 390 °C (DNI = 850 W/m^2, $\dot{m}$ = 3 kg/s). Conversely, increasing the mass flow rate slightly reduces heat loss by moderating absorber temperatures. For instance, Q_{loss} decreases from 226.7 W/m at 3 kg/s to 218.2 W/m at 6 kg/s under identical conditions.

Under vacuum, radiation accounts for nearly all heat loss, as confirmed by the near equivalence of total and radiative losses. With hydrogen in the annulus space, however, convection contributes more prominently, slightly reducing radiation's relative share.

5.5. Influence of wind speed and operational envelope

To capture the combined influence of solar input, operating temperature, and flow rate, two representative extreme conditions were further analyzed, considering the effect of the wind speed:

- a low DNI, lower inlet temperature, and higher mass flow rate case (DNI=850 W/m^2, T_{in} = 290 °C, $\dot{m}$ = 6 kg/s), and
- a high DNI, higher inlet temperature, and lower mass flow rate case (DNI=1000 W/m^2, T_{in} = 390 °C, $\dot{m}$ = 3 kg/s).

These two points effectively bound the practical operational envelope of the parabolic-trough receiver and enable evaluation of wind effects under both mild and severe thermal loading conditions.

The wind-sensitivity analysis was performed for wind speeds of 0, 5, and 10 m s^{-1} under both vacuum and hydrogen annulus conditions. The external convective coefficient was modified according to Eq. (16), and total losses were recalculated for extreme operating conditions. The results, summarized in Table 5, show that increasing wind speed slightly increases the total heat loss but markedly reduces the glass temperature. This behavior is more pronounced for hydrogen, where convective coupling in the annular gap is stronger. For example, under hydrogen at DNI = 1000 W/m^2, $T_{go,\text{avg}}$ decreases from 142.5 °C (no wind) to 70.7 °C (wind speed equal to 10 m s^{-1}), while the total linear loss rises from 723 to 851 W/m, which corresponds to an increase of 18%. In contrast, for the vacuum cases, the increase in thermal loss between the no-wind and 10 m/s wind scenarios was less than 4%. Although the increase in Q_{loss} represents a minor efficiency penalty, the significant reduction in T_{go} is beneficial for receiver durability and thermal safety. From this perspective, the assumption of no wind in this work can be considered as conservative.

6. Conclusions

This study presents a comprehensive numerical investigation of the heat transfer and thermal behavior in parabolic trough receivers under realistic operating conditions, conducted using ANSYS Fluent. The analysis compares vacuum and low-pressure hydrogen environments in the annulus space between the absorber and glass envelope of the receivers. Parametric analysis across mass flow rates (3–6 kg/s), inlet fluid temperatures (290-390 °C), and DNI levels (800–1000 W/m^2) demonstrates the system's sensitivity to these variables. Increasing the mass flow rate from 3 kg/s to 6 kg/s reduces the maximum circumferential temperature difference of the absorber surface (ΔT_{max}) by 40.4%, from 39.4 °C to 23.5 °C (at T_{in} = 290 °C and DNI = 1000 W/m^2).

Table 5
(Q_{loss}) and ($T_{go,avg}$) under different wind speeds, DNI, and flow rates.

DNI	u_w	T_{in}	$\dot{m}$	$T_{go,avg}$ (°C)		Q_{loss} (W/m)	
(W/m^2)	(m/s)	(°C)	(kg/s)	Vacuum	Hydrogen	Vacuum	Hydrogen
850	No wind	290	6	46.1	104.7	95.4	430.9
	5			31.6	62.5	98.6	500.3
	10			29.7	52.7	98.9	515.5
1000	No wind	390	3	72.8	142.5	230.9	723.2
	5			42.5	86.2	237.1	824.6
	10			37.4	70.7	237.8	850.5

Similarly, higher inlet temperatures enhance absorber's temperature distribution uniformity, further lowering ΔT_{max}.

Temperature contours and velocity profiles reveal that higher mass flow rates lower receiver temperatures and centralize flow patterns due to dominant turbulent forces. Additionally, hydrogen in the annulus slightly lowers absorber surface temperatures while increasing glass envelope temperatures by up to 142 °C through convective and conductive heat transfer.

Heat loss analysis shows hydrogen in the annulus increases thermal losses by 3 times compared to vacuum conditions. For instance, at $\dot{m}$ = 3 kg/s and T_{in} = 390 °C, heat loss rises from 230.9 W/m (vacuum) to 723.2 W/m (hydrogen). These results emphasize the necessity of maintaining high-vacuum conditions to minimize energy dissipation.

Wind-speed analysis further revealed that external flow effects slightly increased total heat losses (up to 18%) while substantially lowering glass envelope temperatures, particularly under hydrogen conditions.

The numerical insights derived in this work enable two practical applications: (a) optimization of mass flow rates and temperature thresholds in commercial PTC plants; and (b) accurate prediction of thermal performance variations in solar fields using thermal oils, particularly during hydrogen permeation events.

CRediT authorship contribution statement

Vinod Kumar: Writing – original draft, Visualization, Validation, Software, Methodology, Investigation, Formal analysis, Data curation. **Stefano Savino:** Writing – review & editing, Supervision, Conceptualization. **Rafael López-Martín:** Writing – review & editing, Validation, Resources. **Loreto Valenzuela:** Writing – original draft, Supervision, Resources, Methodology, Investigation, Funding acquisition, Formal analysis, Conceptualization.

Declaration of competing interest

The authors declare that they have no known competing financial interests or personal relationships that could have appeared to influence the work reported in this paper.

Acknowledgments

The authors thankfully acknowledge the funding received from the Spanish government (MCIN/AEI/10.13039/501100011033) to the project Si-CO (Ref. PCI2020-120704-2) under the CSP ERANET Cofund program. CSP-ERA.NET is supported within the EU Framework Programme for Research and Innovation HORIZON 2020 (Cofund ERANET Action, N° 838311).

Appendix A

See Table A.6.

Table A.6
Average temperature of outer surface of receiver T_{ro} and glass cover T_{go}.

$\dot{m}$	T_{in}	Vacuum		Hydrogen		Vacuum		Hydrogen	
(kg/s)	(°C)	850 (W/m^2)	1000 (W/m^2)	850 (W/m^2)	1000 (W/m^2)	850 (W/m^2)	1000 (W/m^2)	850 (W/m^2)	1000 (W/m^2)
		$T_{ro,avg}$ (°C)		$T_{ro,avg}$ (°C)		$T_{go,avg}$ (°C)		$T_{go,avg}$ (°C)	
3	290	304.3	306.7	303.0	305.5	47.2	47.7	106.4	107.2
	310	324.0	326.3	322.6	325.1	51.3	51.8	113.1	113.9
	330	343.6	345.9	342.2	344.6	55.8	56.4	119.9	120.8
	350	363.3	365.5	361.8	364.1	60.7	61.4	127.0	127.8
	370	382.9	385.1	381.4	383.7	66.1	66.8	134.2	135.1
	390	402.7	404.8	401.1	403.3	72.1	72.8	141.7	142.5
4	290	301.8	303.7	300.7	302.8	46.7	47.1	105.6	106.3
	310	321.5	323.4	320.4	322.4	50.8	51.2	112.3	113.0
	330	341.2	343.1	340.0	342.0	55.2	55.7	119.1	119.9
	350	360.9	362.7	359.7	361.6	60.1	60.6	126.2	126.9
	370	380.6	382.4	379.4	381.3	65.5	66.0	133.4	134.1
	390	400.4	402.1	399.1	400.9	71.4	72.0	140.9	141.6
5	290	300.1	301.8	299.2	301.0	46.4	46.7	105.1	105.7
	310	319.9	321.5	318.9	320.6	50.4	50.8	111.8	112.4
	330	339.6	341.2	338.6	340.3	54.8	55.3	118.6	119.2
	350	359.4	360.9	358.3	360.0	59.7	60.2	125.7	126.3
	370	379.1	380.6	378.0	379.6	65.1	65.5	132.9	133.5
	390	398.9	400.4	397.7	399.4	70.9	71.4	140.4	141.0
6	290	299.0	300.4	298.1	299.7	46.1	46.5	104.7	105.3
	310	318.7	320.1	317.8	319.4	50.2	50.5	111.4	111.9
	330	338.5	339.9	337.6	339.1	54.6	55.0	118.3	118.8
	350	358.3	359.6	357.3	358.8	59.4	59.8	125.3	125.8
	370	378.0	379.3	377.0	378.5	64.8	65.2	132.5	133.1
	390	397.9	399.1	396.8	398.2	70.6	71.1	140.0	140.6

Appendix B. Supplementary data

Supplementary material related to this article can be found online at https://doi.org/10.1016/j.applthermaleng.2026.129832.

Data availability

Data will be made available on request.

References

[1] A. Fernández-García, E. Zarza, L. Valenzuela, M. Pérez, Parabolic-trough solar collectors and their applications, Renew. Sustain. Energy Rev. 14 (7) (2010) 1695–1721.

[2] V. Kumar, S. Savino, C. Nonino, Effect of height and position of inner rectangular longitudinal fins in parabolic trough solar receivers, Comput. Therm. Sci.: Int. J. 17 (3) (2025) 1–11.

[3] G. Espinosa-Rueda, J.L. Navarro Hermoso, N. Martínez-Sanz, M. Gallas-Torreira, Vacuum evaluation of parabolic trough receiver tubes in a 50 MW concentrated solar power plant, Sol. Energy 139 (2016) 36–46.

[4] R. Forristall, Heat Transfer Analysis and Modeling of a Parabolic Trough Solar Receiver Implemented in Engineering Equation Solver, Tech. Rep. NREL/TP-550-34169, National Renewable Energy Laboratory (NREL), Golden, CO, 2003.

[5] R.V. Padilla, G. Demirkaya, D.Y. Goswami, E. Stefanakos, M.M. Rahman, Heat transfer analysis of parabolic trough solar receiver, Appl. Energy 88 (12) (2011) 5097–5110.

[6] S.A. Kalogirou, A detailed thermal model of a parabolic trough collector receiver, Energy 48 (1) (2012) 298–306.

[7] Z. Wu, S. Li, G. Yuan, D. Lei, Z. Wang, Three-dimensional numerical study of heat transfer characteristics of parabolic trough receiver, Appl. Energy 113 (2014) 902–911.

[8] J. Guo, X. Huai, Z. Liu, Performance investigation of parabolic trough solar receiver, Appl. Therm. Eng. 95 (2016) 357–364.

[9] F. Burkholder, M. Brandemuehl, H. Price, J. Netter, C. Kutscher, E. Wolfrum, Parabolic trough receiver thermal testing, in: Proceedings of the ASME 2007 Energy Sustainability Conference, 2007, pp. 961–970.

[10] F. Burkholder, C. Kutscher, Heat-Loss Testing of Solel's UVAC3 Parabolic Trough Receiver, Tech. Rep. NREL/TP-550-42394, National Renewable Energy Lab. (NREL), Golden, CO (United States), 2008.

[11] D. Lei, Q. Li, Z. Wang, J. Li, J. Li, An experimental study of thermal characterization of parabolic trough receivers, Energy Convers. Manage. 69 (2013) 107–115.

[12] J.M. Márquez, R. López-Martín, L. Valenzuela, E. Zarza, Test bench HEATREC for heat loss measurement on solar receiver tubes, AIP Conf. Proc. 1734 (1) (2016) 030025.

[13] G.L. Harding, Helium permeation in all-glass tubular evacuated solar energy collectors, Sol. Energy Mater. 5 (1981) 141–147.

[14] K.F. Beckers, G.C. Glatzmaier, Addressing solar power plant heat transfer fluid degradation: Experimental measurements of hydrogen transport properties in binary eutectic biphenyl/diphenyl ether, Sol. Energy 173 (2018) 304–312.

[15] J. Li, Z. Wang, D. Lei, J. Li, Hydrogen permeation model of parabolic trough receiver tube, Sol. Energy 86 (2012) 1187–1196.

[16] X. Olano, A.G. de Jalón, D. Pérez, J.G. Barberena, J. López, M. Gastón, Outcomes and features of the inspection of receiver tubes (ITR) system for improved O&M in parabolic trough plants, AIP Conf. Proc. 2033 (1) (2018) 030011.

[17] H. Price, M.J. Hale, R. Mahoney, C. Gummo, R. Fimbres, R. Cipriani, Developments in high temperature parabolic trough receiver technology, in: Proceedings of the ASME 2004 International Solar Energy Conference, ISEC2004, 2004, pp. 659–667.

[18] P. Alamdari, M. Khatamifar, W. Lin, Heat loss analysis review: Parabolic trough and linear Fresnel collectors, Renew. Sustain. Energy Rev. 199 (2024) 114497.

[19] B. Kalidasan, M.A. Hassan, A.K. Pandey, S. Chinnasamy, Linear cavity solar receivers: A review, Appl. Therm. Eng. 221 (2023) 119815.

[20] V. Kumar, C. Nonino, S. Savino, On the improvement of the thermal performance of longitudinally finned parabolic trough solar receivers, Appl. Therm. Eng. 279 (2025) 127840.

[21] F. Burkholder, C. Kutscher, Heat Loss Testing of Schott's 2008 PTR70 Parabolic Trough Receiver, Tech. Rep. NREL/TP-550-45633, National Renewable Energy Lab. (NREL), Golden, CO (United States), 2009.

[22] E. Setien, R. López-Martín, L. Valenzuela, Methodology for partial vacuum pressure and heat losses analysis of parabolic troughs receivers by infrared radiometry, Infrared Phys. Technol. 98 (2019) 341–353.

[23] S. Caron, M. Röger, In-situ heat loss measurements of parabolic trough receivers based on transient infrared thermography, Sol. Energy 135 (2016) 111–121.

[24] M.E. Carra, E. Setién, L. Valenzuela, R. López-Martín, C. Amador, S. Caron, J. Ballestrín, J. Fernández-Reche, J.A. Carballo, A. Ávila-Marín, Study of parameters influence on the measurement of vacuum level in parabolic trough collectors' receivers using infrared thermography, Infrared Phys. Technol. 131 (2023) 104657.

[25] A. Oufadel, M.E. Ydrissi, A.A. Hassani, H. Ghennioui, A. Ghennioui, E. Ghali bennouna, A.E. Amri, F. Abdi, In-situ heat losses measurements of parabolic trough receiver tubes based on infrared camera and artificial intelligence, Environ. Chall. 10 (2023) 100679.

[26] M.-A. Pérez-Cutiño, A. Pikrakis, J.-M.D.-B. nez, J. Valverde, Meta-learning with hypernetworks: Cost-effective fault detection in parabolic trough plants, Eng. Appl. Artif. Intell. 133 (2024) 108492.

[27] H. Price, R. Forristall, T. Wendelin, A. Lewandowski, T. Moss, C. Gummo, Field survey of parabolic trough receiver thermal performance, in: Proceedings of the ASME 2006 International Solar Energy Conference, ISEC2006, 2006, pp. 109–116.

[28] T. Kraft, G. Bern, S. Rohani, M. Schmitz, W. Platzer, Vacuum loss detection of PTC in CSP plants via temperature-sensors, in: SolarPACES Conference Proceedings, vol. 2, 2024.

[29] G.C. Glatzmaier, Hydrogen measurement & extraction at Nevada solar one, in: SolarPACES Conference Proceedings, vol. 2, 2024.

[30] D. Lei, Y. Ren, Z. Wang, Numerical study of conduction and radiation heat losses from vacuum annulus in parabolic trough receivers, Front. Energy 16 (2022) 1048–1059.

[31] İ.H. Yılmaz, A. Mwesigye, Modeling, simulation and performance analysis of parabolic trough solar collectors: A comprehensive review, Appl. Energy 225 (2018) 135–174.

[32] A. Mwesigye, İ.H. Yılmaz, J.P. Meyer, Numerical analysis of the thermal and thermodynamic performance of a parabolic trough solar collector using SWCNTs-Therminol®VP-1 nanofluid, Renew. Energy 119 (2018) 844–862.

[33] J.O. Hirschfelder, C.F. Curtiss, R.B. Bird, Molecular Theory of Gases and Liquids, John Wiley & Sons, New York, 1954.

[34] National Renewable Energy Laboratory, Concentrating solar power projects – SolarPACES, 2025, https://solarpaces.nrel.gov/. (Accessed 14 October 2025).

[35] M. Botejara-Antúnez, J. González-Domínguez, F.J. Rebollo-Castillo, J. García-Sanz-Calcedo, Life cycle and environmental impact assessment of heat transfer fluids in parabolic trough CSP plants, Sustain. Energy Technol. Assess. 74 (2025) 104188.

[36] Eastman Chemical Company, Eastman product finder: Heat transfer fluids, 2025, https://www.eastman.com/en/products/product-finder. (Accessed 14 October 2025).

[37] Therminol® VP-1 heat transfer fluid, 2025, URL https://www.therminol.com/product/71093459. (Accessed 02 May 2025).

[38] Therminol® VP-1 heat transfer fluid: Product technical data sheet, 2025, URL https://www.eastman.com/content/dam/eastman/corporate/en/literature/t/tf9141.pdf. (Accessed 02 May 2025).

[39] Ansys Inc., Ansys Fluent User's Guide, Release 2025 R1, Ansys, Inc., Canonsburg, Pennsylvania, USA, 2025, https://www.ansys.com.

[40] F.R. Menter, Two-equation eddy-viscosity turbulence models for engineering applications, AIAA J. 32 (8) (1994) 1598–1605.

[41] Z. Tu, D. Piccioni Koch, N. Sarunac, M. Frank, J. Mao, Thermal analysis of a solar external receiver tube with a novel component of guide vanes, Energies 14 (8) (2021).

[42] M.A. Khuda, J. Khalesi, Z. Tu, Y. Long, D. Piccioni Koch, N. Sarunac, Numerical analysis of a developing turbulent flow and conjugate heat transfer for molten salt and liquid sodium in a solar receiver, Appl. Therm. Eng. 217 (2022) 119156.

[43] Z.D. Cheng, Y.L. He, F.Q. Cui, R.J. Xu, Y.B. Tao, Numerical simulation of a parabolic trough solar collector with nonuniform solar flux conditions by coupling FVM and MCRT method, Sol. Energy 86 (2012) 1770–1784.

[44] S. Anand, S. Kumar, Optimization of gaseous working fluid and internally finned absorber tube for enhancing the thermal performance of parabolic trough solar collector, Appl. Therm. Eng. 239 (2024) 122078.

[45] Ansys Inc., Ansys Fluent Theory Guide, Release 2025 R1, Ansys, Inc., Canonsburg, Pennsylvania, USA, 2025, https://www.ansys.com.

[46] P. Wang, D.Y. Liu, C. Xu, Numerical study of heat transfer enhancement in the receiver tube of direct steam generation with parabolic trough by inserting metal foams, Appl. Energy 102 (2013) 449–460.

[47] V. Dudley, G. Kolb, A. Mahoney, T. Mancini, C. Matthews, M. Sloan, D. Kearney, Test Results: SEGS LS-2 Solar Collector, Tech. Rep. SAND94-1884, SANDIA National Laboratories, 1994.

[48] B. Petukhov, Heat transfer and friction in turbulent pipe flow with variable physical properties, in: Advances in Heat Transfer, vol. 6, Elsevier, 1970, pp. 503–564.

[49] V. Gnielinski, New equations for heat and mass transfer in turbulent pipe and channel flow, Int. Chem. Eng. 16 (2) (1976) 359–368.

[50] L. Valenzuela, R. López-Martín, C.M. Amador-Cortés, C. Hilgert, Experimental heat losses in hydrogen-doped parabolic trough receivers, in: SolarPACES Conference Proceedings, vol. 3, 2024.